SAND2019-5870C

Response of Jointed-Structures in a Shock Tube: Simultaneous PSP and DIC with Comparison to Modeling

Kyle P. Lynch[1], Elizabeth M. Jones[2], Adam R. Brink[2], Daniel R. Roettgen[2], Robert J. Kuether[2], Justin L. Wagner[3]
Sandia National Laboratories, Albuquerque, NM 87185

Allen Mathis[4], D. Dane Quinn[5]
Akron University, Akron, OH 44325

Experiments and modeling were used to study the nonlinear dynamics of a jointed-structure in a shock tube. The structure was a full-span square cylinder with internal bolted connections excited by vortex shedding. The Reynolds number based on cylinder width was ≈ 10^5. The cylinder was exposed to an impulsive force associated with the incident shock followed by transverse loading imposed by vortex shedding. In the experiment, aerodynamic loading was characterized with high-speed pressure sensitive paint (PSP) while digital image correlation (DIC) concurrently measured the structural response. The maximum displacement occurred when the vortex shedding frequency most closely matched the structural mode of the beam associated with rocking motion at the joint. A finite element model was developed using Abaqus, where the nonlinear joint dynamics were simulated using Coulomb friction. The PSP data loaded the model and the interaction was treated as one-way coupled. The simulations well-matched the trends observed in the experiment. The overall agreement on transverse displacements was on average 24%. The modeling showed rocking about the joint during vortex shedding was critical to the nonlinear damping and energy dissipation in the structure. Collectively, this experimental-modeling campaign highlights the importance of jointed-connections to energy dissipation under aerodynamic loading.

I. Introduction

Fluid-structure interaction (FSI) in unsteady fluid dynamic environments can lead to significant uncertainties in predictions of structural response. Although a fair amount of FSI work has been conducted in low-speed flows e.g., [1], the availability of data in high-speed, compressible flows remains scarce. A few notable examples include the structural response of a store in an aircraft bay [2], panel response under loading imposed by boundary layers [3-5], panels subjected to shock wave-boundary layer interactions [6-8] and panel response to supersonic jets. In the latter cases, attention is often given to large panel displacements (approx. panel thickness), where the structural dynamics become nonlinear [7-11].

As nonlinearities are excited in the structural response, the difficulties in predicting the behavior of systems undergoing FSI are compounded. The resulting behavior is highly sensitive to the fluid excitation, which can likewise be dependent on the structural response. In the present work an additional complication is introduced due to the presence of mechanical joints, that is, mechanical connections between structural components. The prediction of energy transfer from the fluid throughout a structure requires understanding of load path effects through mechanical connections. In comparison to their monolithic counterparts, which are appropriately modeled using linear structural dynamics, jointed structures exhibit increased energy dissipation and decreased vibrational loads [12-14]. Moreover,

[1] Senior Member of the Technical Staff, Engineering Sciences Center, Member AIAA, klynch@sandia.gov.
[2] Senior Member of the Technical Staff, Engineering Sciences Center.
[3] Principal Member of the Technical Staff, Engineering Sciences Center, Senior Member AIAA, jwagner@sandia.gov.
[4] Graduate Research Assistant, Department of Mechanical Engineering.
[5] Professor, Department of Mechanical Engineering.

the dynamics of jointed structures are highly sensitive to the interface parameters, such as the coefficient of friction between surfaces and the normal loads arising from bolted connections. Thus, improperly modeling joints may lead to inaccurate structural models and ultimately overly conservative designs. Currently, semi-empirical constitutive models are often used, based on gross parameters such as joint stiffness, the initiation force required for macro-slip, and effective damping coefficients determined from overall energy dissipation. Such parameters can be measured by specific harmonic loading experiments using mechanical devices such as an impact hammer or a shaker table [15-17], However, when a structure experiences a different loading environment, the effective dissipation parameters change. Therefore, when a system is placed in an environment such as a flow containing unsteady air-shocks, vortex shedding, aeroacoustics, and turbulence, it is forced in a way differently from the mechanical methods used to calibrate the models and the numerical model may no longer be predictive. Ultimately, semi-empirical models for joints and interfaces may lead to incorrect estimates of vibrations in structures subjected to fluid-dynamic loadings due to inappropriate calibration of equivalent parameters.

This hypothesis motivates the present experimental and modeling campaign capable of producing and measuring the relevant fluid and structural dynamic physical phenomena present in high-speed FSI and predicting such behavior through computational models. The approach is to drive gas-phase shock waves traveling at approximately 500 m/s into canonical jointed-structures designed to exhibit a nonlinear response. Following an impulsive starting load, an unsteady wake is established in the shock-induced flow. The vortex shedding exerts a transverse loading on the structure. Additionally, stochastic forcing is present due to smaller-scale turbulent fluctuations in the wake. Therefore, a physically rich fluid dynamic loading environment exists to drive the FSI, which can be used to test the fidelity of existing nonlinear structural dynamics models.

Simultaneous high-speed measurements of aerodynamic loading and structural response are required to create a model validation dataset; however, the small size of the tested structures herein (height of ≈ 13 mm) precludes the use of traditional transducers and accelerometers. Further, single-point measurements make model validation difficult because they cannot fully resolve structural mode shapes or complex pressure fields. Fortunately, high-speed, full-field alternatives are available. PSP is becoming prevalent in high-speed aerodynamics [19, 20] and DIC in high-speed FSI is gaining popularity [8, 10, 20-23].

The present work uses high-speed PSP and DIC simultaneously by placing the DIC speckle pattern overlaid on PSP. This presents challenges as aero-optical distortions associated with shock waves, turbulence, and shock-heated gas contribute to measurement noise. Additionally, since the DIC speckle is overlaid on the PSP, the DIC pattern must be filtered out to properly post-process the PSP data. Finally, high-precision DIC is required to capture the structural displacements that are as small as 5 microns. The shock tube data are obtained at a variety of flow conditions including cases where a natural frequency of the jointed-beam is near the vortex shedding frequency. This dataset is then used to evaluate a model incorporating nonlinear energy dissipation at the joints.

The structural response of the beam is subsequently simulated using one-way-coupled structural dynamics, where the aerodynamic loading obtained via the PSP is used directly as the forcing input. The predicted response is compared to the experimental data to assess the viability of the Coulomb friction model [24, 25] to assess load path effects.

II. Experimental Arrangement

A. Shock Tube Facility

Experiments are performed in the Multiphase Shock Tube (MST) at Sandia National Laboratories, described in detail in [26] and shown in Fig. 1. Briefly, the MST is a shock tube with a driver section consisting of a circular pipe 89 mm in diameter that is 2.1 m long. The driver is pressurized with air at room temperature. The driven section is a square cross-section pipe of 79 mm height and width, with a length of 5.9 m. It is filled with ambient air at room temperature and atmospheric pressure of 84.1 kPa. The test section is located approximately 4.9 m downstream of the valve and is a specialized square section with optical access via fused silica glass windows on all sides. The top and bottom portions have solid inserts and provide the mounting points for the beam. Fused-silica windows running the length of the test section with a height of 25 mm are used to image the experiment.

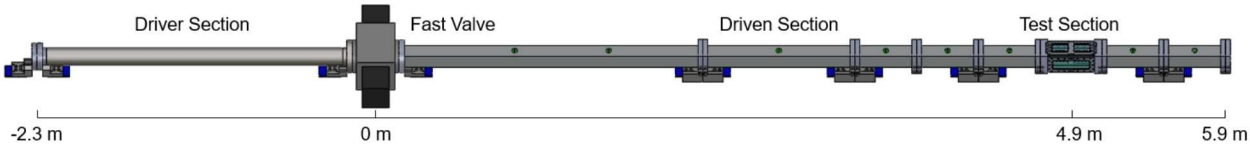

Fig. 1 Diagram of multiphase shock tube with fast-acting valve.

A Dynamics Systems Research (model 725-3.0-6000) fast acting valve acts as the diaphragm. The valve is actuated using an independent pressure source, allowing for a continuous range of driver pressure conditions. Further, the valve is electronically triggered to allow for synchronization with light source and camera equipment. The continuous range of conditions allows the strength of the structural loading to be widely varied.

Six driver pressures P_4 are used to span the range of flow conditions described in Table 1. The conditions are determined by measuring the shock Mach number M_s in the test section with fast-response PCB pressure transducers (model 113B27, 100 psi range). Unsteady wave theory is used to calculate the induced properties in the freestream including velocity U_∞, Mach number M_∞, dynamic pressure q_∞ and Reynolds number based on beam width Re_D. The test time at each condition is about 5 milliseconds (ms). In all cases the reflected shock wave arrives prior to the driver gas contact surface. The vortex shedding frequency f_{shed} and the associated Strouhal number St_D ($f_{shed} \times D / U_\infty$) are determined by the PSP as is described subsequently. Owing to boundary layer effects [27], the velocity increases during a test by as much as ≈ 12% for the higher driver pressure conditions [28]. The Strouhal number is based on the average velocity to incorporate this effect. Each condition was run four times to quantify precision uncertainty.

Table 1: Mean Experimental Conditions

P_4 (psi)	M_s	U_∞ (m/s)	M_∞	q_∞ (kPa)	Re_D	f_{shed} (kHz)	St_D
50	1.30 ± 0.01	153	0.41	19	9.12×10^4	1.76	0.14
75	1.34 ± 0.01	173	0.45	27	1.01×10^5	1.98	0.14
100	1.39 ± 0.01	191	0.50	37	1.11×10^5	2.20	0.13
125	1.42 ± 0.01	206	0.53	44	1.17×10^5	2.86	**0.16**
150	1.45 ± 0.01	219	0.56	52	1.23×10^5	3.08	**0.16**

B. Test Model

A steel (4340 alloy) specimen with a 12.7 × 12.7 mm^2 cross-section was designed to exhibit a nonlinear response when subjected to an impulsive loading (Fig. 2). Finite element analysis (FEA) was used to ensure that a natural frequency of the beam sensitive to vortex shedding would be active near the anticipated vortex shedding frequencies. The model consists of a back plate containing two threaded interfaces on raised flanges. These bolts connect to a flange on a thin shell. The pressure loading on the faces of the shell is transferred through to the internal bolted joint, causing a localized strain and slip that is nonlinear depending on the input loading. Further, rotation of the shell about this joint can occur under asymmetric loading imposed by vortex shedding. The pressure is measured using PSP on all three of the painted shell faces of Fig. 2. DIC is measured only on the front face visible by both cameras.

The back plate of the beam is connected directly to the shock tube using UNF ¼"-28 bolted connections, torqued to 100 in-lbs. This was verified to be a sufficient torque level to prevent measurable slippage of this bolted connection during the experiment. The internal bolts are UNF #3-56, torqued to 8.0 ± 0.5 inch-pounds. The intent was to have the back plate be essentially rigid; however, as discussed subsequently, the structural dynamics of the back plate do affect the interaction. The shell piece is 2.5 mm shorter than the back plate, preventing contact between the shell and the shock tube walls as the shell undergoes motion.

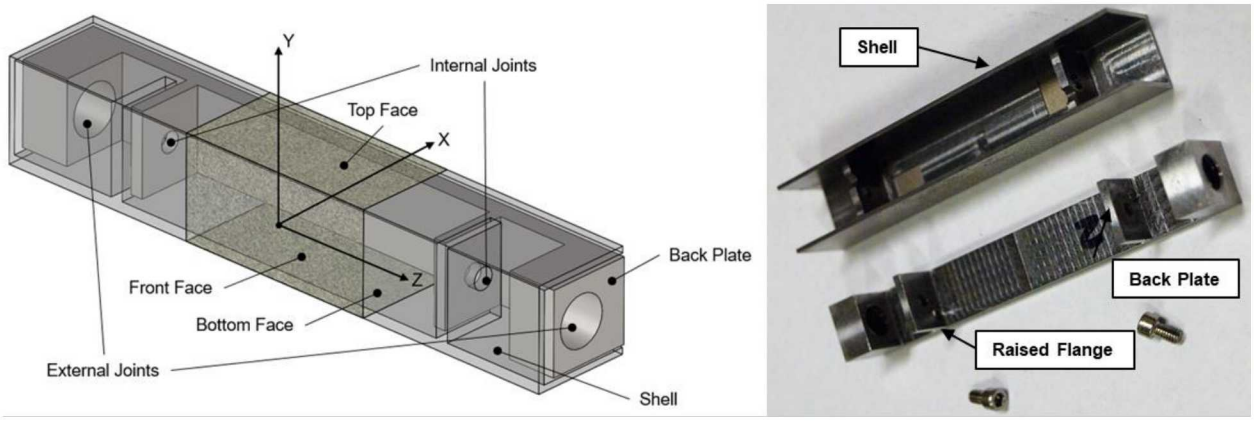

Fig. 2 Model beam: a) schematic and b) photo showing the beam disassembled.

The full-span beam assembly is mounted in a vertical orientation within the shock tube; the resulting coordinate system is defined in Fig. 2. The origin is located on the center of the front face of the beam. Displacements in x correspond to a response generated from a front face pressure, and y-displacements correspond to responses from asymmetric pressure loading on the top and bottom face. As expected, the z-displacements are minimal and are omitted herein.

C. Optical Setup

A stereo imaging configuration is used as shown in Fig. 3. Phantom v2512 high speed cameras are used for imaging (28 μm pixels, 1280 x 800 px at 20 kHz). A cropped image size of 896 x 512 is used for this experiment, while the frame rate is maintained at 20 kHz. An exposure time of 49 μs captures sufficient signal from the PSP. A pair of Nikon 105 mm lenses are used with LaVision Scheimpflug mounts, allowing a low f/# = 5.6 to capture additional signal while aligning the focal plane with the front face of the beam. The field-of-view captured the center 25 mm of the front face of the beam in both camera systems. The center portion of top and bottom faces of the beam (shaded region in Fig. 2a) is captured independently in the two separate cameras. Note that viewing of the entire beam span was precluded by the 25-mm tall test section windows. The physical scaling of the system is 15.6 px/mm. At f/# = 5.6, the depth-of-field is smaller than the depth of the beam even with the Schiempflug mounts. Therefore, as a compromise between the DIC on the front surface and the PSP on the top and bottom faces, the focus plane is set slightly behind the front face of the beam, so that the top and bottom beam faces are also within the depth-of-field. The cameras are mounted on a set of optical rails to adjust the stereo angle and working distance. The stereo-angle, defined as the total angle between the lenses, is approximately 60º and the stand-off distance is approximately 200 mm. The cameras systems are mounted to a large floating vibration isolation table to reduce propagation of shock tube motion through to the cameras.

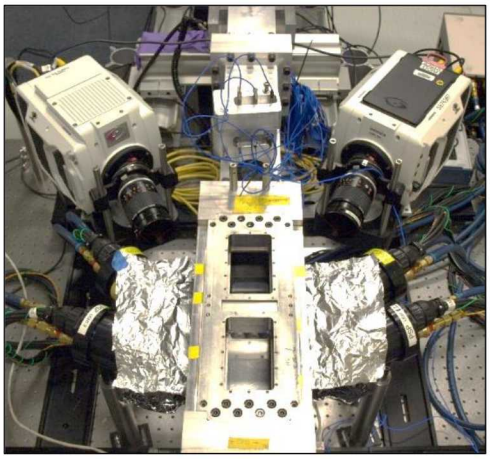

Fig. 3 Photo of optical setup.

D. Pressure Sensitive Paint

The PSP uses a formulation recently proposed by Egami et al. [29]. A ruthenium luminiphore ($Ru(dpp)_3$) is mixed within a silicone rubber (RTV) binder containing nanoscale boron nitride particles. The particles provide a porous surface for interaction with surrounding oxygen, yielding a time response of approximately 12 μs. The three constituents are mixed following an 80% particle-to-(polymer+particle) weight ratio using toluene as a solvent:

$Ru(dpp)_3$: polymer : particle : toluene = 3 mg : 60 mg : 240 mg : 10mL

The formulation is stirred for two hours using a magnetic stirrer and applied using an airspray gun. The paint cures for four hours in a vacuum chamber prior to an experiment. Notably, unlike sprayable fast-PSP based on platinum-tetra-fluoro-phenyl-porphrin (PtTFPP) requiring a two-part application procedure, this paint is applied in one step.

Illumination is provided by two ISSI LM2XX-DM-400 and two ISSI LM2XX-DM-460 water-cooled LED arrays, each outputting between 8-12 W at 400 ± 17 and 460 ± 31 nm, respectively. The light enters the test section via the same side windows used for imaging. The paint excitation wavelength peaks at 475 nm, and emits at a center wavelength of 600 nm, allowing a 590 nm long-pass filter to remove excitation light.

The Stern-Volmer ratiometric method is used to convert image intensities to pressures (see e.g. [30]). The in-situ calibration of [29] found a pressure sensitivity of 0.62%/kPa and temperature sensitivity of 1.05%/ºC for this formulation. This temperature sensitivity is significantly less than PtTFPP, which is particularly advantageous for use in a shock tube where there is a temperature rise after the shock.

The calibration process is as follows. The 'wind-off' image I_0 is compiled from the average of 10 acquired images before the arrival of the shock wave and the ratio I_0/I is compiled for each subsequent image. An initial intensity ratio $(I_0/I)_0$ is calculated from an average of 10 ratios before the incident shock arrives. A final intensity ratio $(I_0/I)_R$ is calculated after the arrival of the reflected shock. The signal is then normalized by these values and multiplied by the pressure after the reflected shock p_R as measured using an external PCB sensor such that pressure P is calculated as follows:

$$P = \frac{P_R(I_0/I)}{(I_0/I)_R - (I_0/I)_0} \tag{1}$$

This effectively corresponds to a linear calibration between the initial ambient pressure and post-reflected shock pressure, which is theoretically identical over all beam surfaces.

An example of a raw image from each camera is shown in Fig. 4. An image registration procedure is required when analyzing PSP to map the images to a physical coordinate system. Furthermore, during a run the beam vibrates and will cause the 'wind-on' images to lose alignment with the reference. This issue is common in wind tunnel facilities and can be corrected using image registration with multiple-markers [31, 32], or lifetime PSP which does not require a wind-off reference [33]. The former is applied in this work. A three-step procedure is therefore used to process the images.

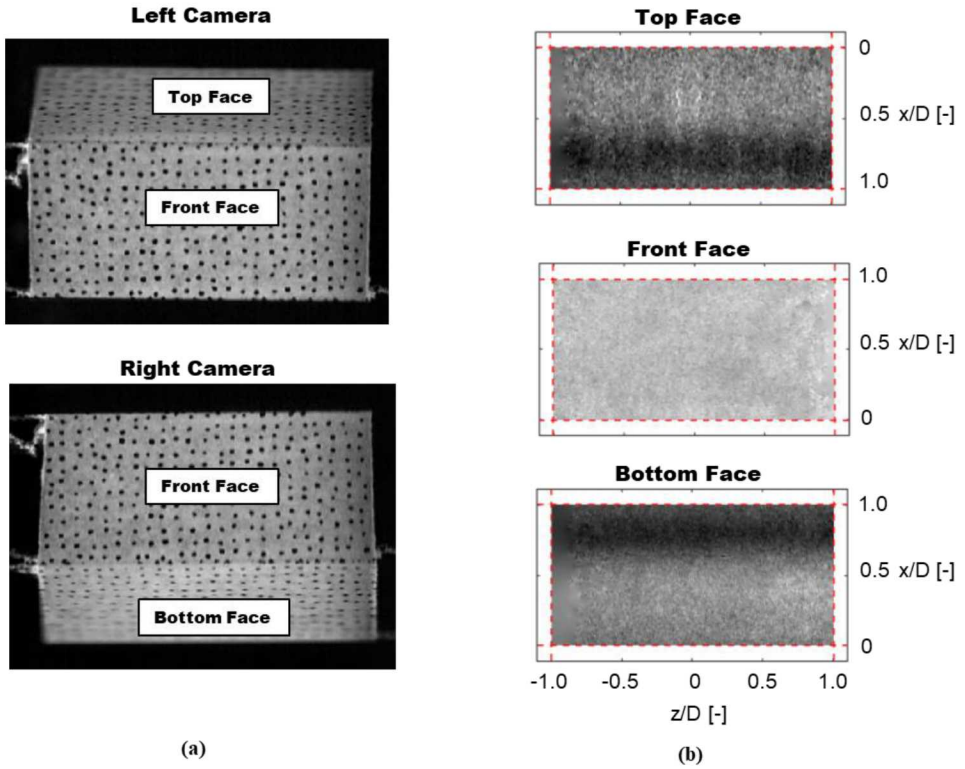

Fig. 4 Comparison of raw images and PSP results: a) raw images from each camera prior to shock arrival and b) unwrapped PSP images with speckle pattern removed and filled. The time of the PSP images corresponds to shock arrival. Note that the PSP intensity has been inverted such that high intensity equates to high pressure.

The first processing step applies a projective transformation to 'unwrap' the raw images from the top, bottom and front of the beam to the known physical coordinates. The projective transform is defined from four points manually identified on each face in the reference image. The second step corrects for small misalignments due to vibrations. The speckle pattern on all sides of the beam is utilized to allow a rigid image registration algorithm to be used for the alignment (Matlab imregister). The last step is to separate the speckle pattern from the PSP signal and fill in the speckle pattern. A simple threshold of 30% of the mean reference image intensity is used to create a mask. Following this, the masked regions are filled using a Laplacian inpainting algorithm (Matlab regionfill). An example of processed PSP images resulting from this three-step process is given in Fig. 4b. Additional details on the PSP processing and image registration can be found in Lynch et al. [26].

E. Digital image correlation

Stereo DIC is used to measure the surface deformation of the front face of the beam as this is the only face that is seen by both cameras (Fig. 4). The speckle pattern is applied on all sides using a simple ink stamp (Correlated Solutions square ink stamp, 0.013 mm dot size). As discussed previously, the speckle pattern on the top and bottom faces is used

only for the PSP image registration and not DIC. The thin layer of ink effectively blocks the UV excitation light from reaching the lumiphores and results in a high-contrast pattern. A sparse speckle pattern is used as a compromise between the optimal speckle density for DIC and maintaining sufficient PSP coverage. In 16-bit quantization, the minimum intensity within the speckles is about 1900 counts and the maximum intensity is about 14000 counts. The image noise level, defined here as standard deviation of the background, is 260 counts. This yields a contrast, defined here as (14000-1900) / 260 = 50, which is found to be sufficient for DIC processing.

Correlated Solutions VIC-3D v8 software is used for calibration and evaluation. Two sets of calibration images are collected, one using a standard dot-grid calibration target and a second using a speckled flat plate that fills the field of view. Approximately 100-200 images are captured of each target as the target is rotated, tilted, and plunged within the field-of-view and depth-of-field of the two optical systems. Correlated Solutions recently introduced a complex camera model (variable ray origin; VRO, 5th order), which takes tangential distortions through windows into account. A hybrid calibration is used. This method uses the correlation results from the speckled plate to calibrate the complex camera model and the dot-grid target to set the scale (pixels to millimeters).

Processing uses a subset size of 35 pixels, a step size of 10 pixels, and an affine subset shape function. Because the beam motion during the experiment has low spatial gradients, a large subset size is used to reduce noise and a large step size reduces processing time. Further, a low-pass spatial filter is applied to the images prior to correlation.

A polynomial fit is applied to the DIC data to remove / detrend large-scale motion/recoil of the shock tube. Finally, independent tests using a rigid beam were used to estimate the measurement uncertainty. These experiments yielded errors of ≈ +/- 3 microns in v and +/- 8 microns in u after the passage of the shock. At the time of shock passage and up until 1.0 ms thereafter, the errors rise to +/- 5 microns in v and +/- 40 microns in u owing to refractive effects [35].

III. Example Experimental Results

A. Pressure Sensitive Paint

Example pressures traces obtained at a driver pressure of 75 psi (Table 1) are shown in Fig. 5a. The pressure traces are averaged over each face and compared to a wall-mounted pressure sensor. The sensor signal has been aligned in time with the arrival of the incident shock even though it is at a location upstream of the beam. This causes the reflected shock to arrive later in time for the sensor signal. Following the incident shock, the pressure rapidly rises on all sides of the beam, with a front face loading approximately twice that of the transverse surfaces. The data are also plotted as a function of normalized time in normalized time $t^* = tU_\infty / D$, which is the appropriate normalization for impulsively started flows. The pressures on the sides of the beam exhibit an in-phase shedding initially and then gradually transition to an out-of-phase shedding for the remainder of the run. This transition occurs at t* ≈ 10, consistent with previous high-speed PIV measurements made in the wake of the cylinder [28]. The vortex shedding is further described in the pressure difference (ΔP) trace shown in Fig. 5b, where a clear periodic forcing is observed. As discussed subsequently, this periodic vortex shedding leads to a substantial transverse fluid dynamic forcing of the beam shell. Finally, the reflected shock arrival at about 5 ms terminates the flow and the vortex shedding.

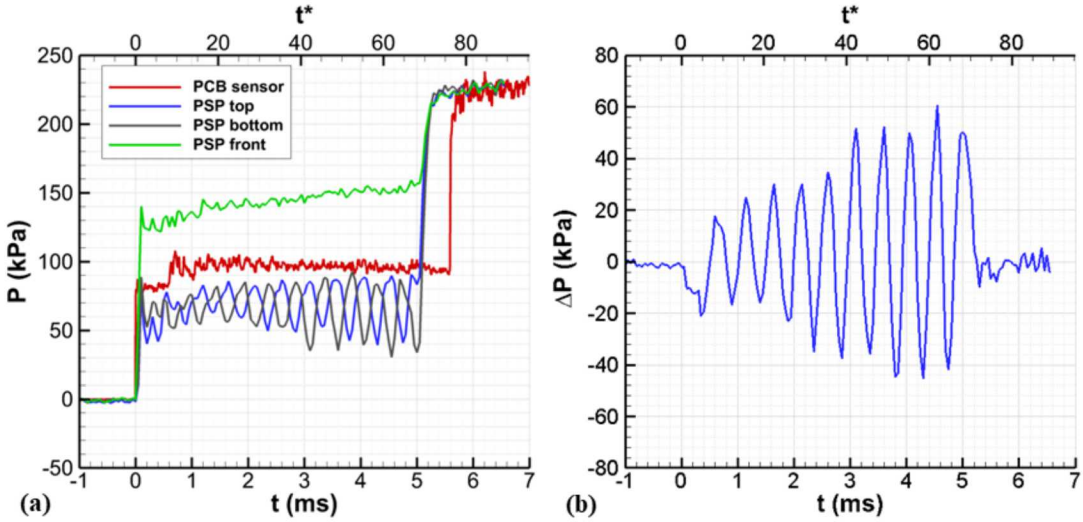

Fig. 5 Pressures during a 75-psi run: a) PSP traces spatially averaged over each face compared to a wall-mounted PCB sensor and b) averaged pressure difference between top and bottom faces.

Example displacement results averaged over the four experiments with a driver pressure of 75 psi are shown in Fig. 6. The displacements correspond to that at the coordinate origin, namely the center of the front face. Displacements are given up to about 0.5 ms prior to the arrival of the reflected shock. Immediately apparent is a strong oscillatory behavior in the v-component caused by vortex shedding (Fig. 6b). The time-varying envelope is less significant as four runs are not enough to statistically resolve envelope trends associated with vortex shedding at high Reynolds numbers [28]. There is also less-pronounced periodic motion in the u-component (Fig. 6a).

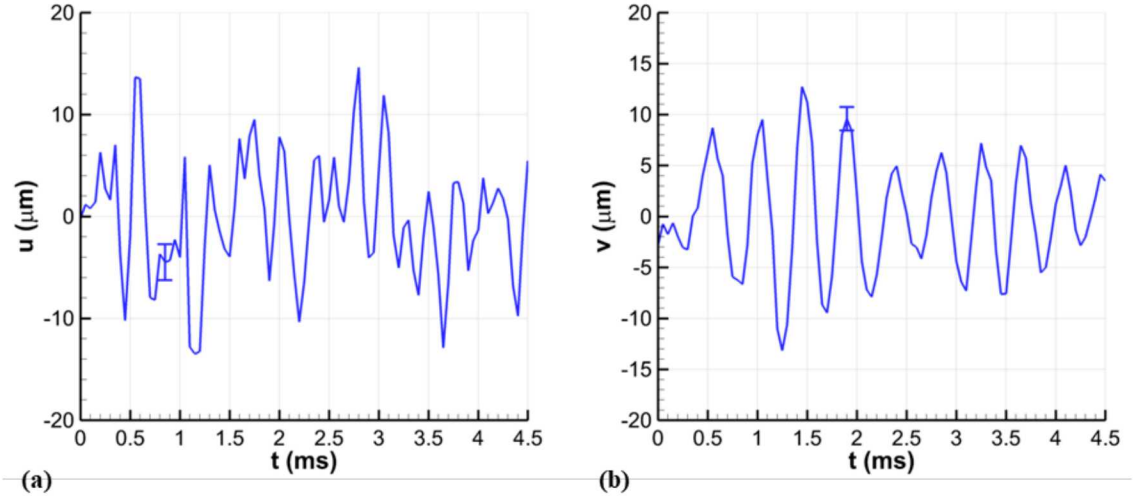

Fig. 6 Example displacements averaged over four runs at a driver pressure of 75 psi: a) u displacement and b) v displacement. Error bars are the standard error.

Proper orthogonal decomposition (POD) is used to visualize the most energetic motions of the beam during the interaction. Such an exercise is particularly useful for subsequent comparison to the finite element modeling. The displacement data $u(x,t)$ is decomposed into a set of spatially-dependent modes $\phi_i(x)$ and time-dependent mode coefficients $a_i(t)$ according to equation 2, where x are the set of spatial coordinates, t is the time, i is the mode index, and the overbar indicates a time-average. Following the procedure in [34], the u-, v-, and w- components are formatted into a single matrix and the Matlab 'pca' function is used to perform the decomposition.

$$u(x,t) - \bar{u}(x) = \sum_i a_i(t)\phi_i(x) \tag{2}$$

The mode shapes $\phi_i(x)$ provide a clearer picture of the underlying beam motion rather than direct inspection of the displacement fields. The first two modes, comprising approximately 60% of the total energy, are shown in Fig. 7. The modes are multiplied by a mode coefficient of -1/+1 (red/blue) to assist visualization of their oscillatory behavior. Mode 1 represents a streamwise translation of the beam. Mode 2 is a rocking mode, where the face of the beam rotates along its central axis and causing a pronounced in the v-component displacement.

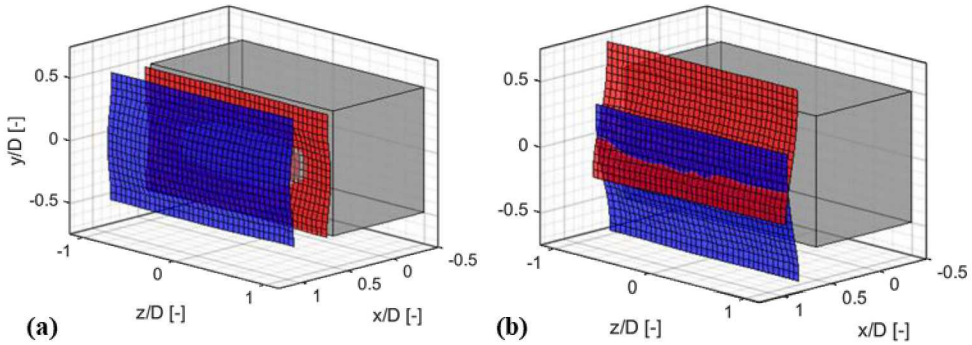

Fig. 7 POD modes of beam displacement: a) mode 1 and b) mode 2. Red and blue represent the mode shapes multiplied by -1 and +1 mode coefficients a_i.

The mode coefficients $a_i(t)$ are time-dependent; plotting their time-series illustrates when the 'translation' or 'rocking' modes are active during the run. Although, not shown here, spectral analysis reveals that the dominant frequency associated with streamwise displacement is consistent with mode 1, whereas the dominant frequency associated with transverse displacement is consistent with mode 2 [35].

IV. Numerical Methods

A finite element model of the system is developed using the Dassault Systemes FEA software Abaqus with the primary goal of investigating the nonlinear structural dynamics of the specimen under complex aerodynamic loading in the shock tube. A secondary goal is to test the performance of the Coulomb friction model in this scenario. The experimental data are utilized to calibrate and validate the model. Several assumptions allow the structural dynamics modeling to be tractable including:

1) The PSP measurements are individually averaged over the three measured surfaces of the specimen to create uniform pressure distributions that served as force inputs to the model. In addition to the assumption of uniform pressure, this assumption assumes that the pressure measured over the middle-third of the beam (Fig. 2), is equivalent across the beam. With continuing time, the sidewall boundary layers grow, which will decrease the validity of this assumption. Specifically, the boundary layer thickness in the higher driver pressure runs is as high as 25% of the beam span on each side [28].
2) The pressure fluctuations on the back plate (i.e., in the turbulent wake) are not measured and are assumed to be negligible to the interaction since the back plate has higher rigidity in comparison to the shell.
3) The FSI is taken to be one-way-coupled.
4) The ¼-28 bolts attaching the beam to the shock tube (Fig. 2) are modeled as perfectly fixed boundaries.

The calculated displacement outputs of the model in response to the known pressure inputs are compared with DIC measurements in the shock tube to validate the simulations. After this assessment, an investigation into the nonlinear dynamical system properties of the system is described to better understand the relationship between the fluid loading and the structural response.

A. Model Development and Verification

A cutaway view exposing the bolt and jointed interface is shown in Fig. 8. Because of the symmetry of the structural specimen and because the PSP measurements are averaged over the individual surfaces of the specimen, the analysis is symmetric about the mid-plane. As a result, symmetry boundary conditions (BCs) are applied. In the experimental setup, it is only possible to capture the pressure on the top, front, and bottom faces; therefore, the pressure on the back face is assumed to be negligible and remain at nominal ambient pressure. Numerical experiments showed that the response was insensitive to variations in the value of *constant* pressure applied on the back face of the beam. Additionally, the outer bolt hole in Fig. 8 is modeled using fixed boundary conditions.

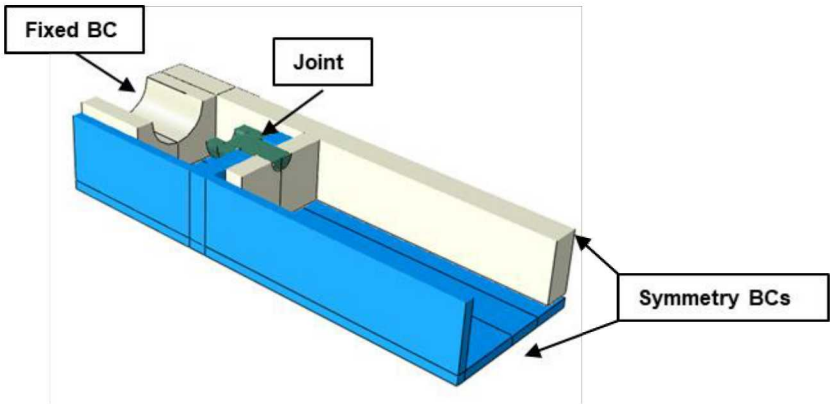

Fig. 8 FEA model geometry taking advantage of symmetry (cutaway-view).

The experimental pressure loading data are applied to the model as external loads that are invariant with the state of the system, i.e. the effect of the vibration of the structure on the surrounding fluid is not considered in this one-way coupled approach. The primary source of nonlinearity in the model is the interface of the bolted connection at the joint

shown in Fig. 8. The friction at the interface is modeled using Coulomb friction. The analysis of the part under fluid dynamic loading is simulated using explicit dynamics. Prior to simulating the shock response, the bolts in the joint are preloaded to capture the correct initial equilibrium state of the model. The typical subroutine for preloading bolts in is unavailable in Abaqus/Explicit. To compensate, the bolt is preloaded in a two-step process as detailed in Mathis [36].

To verify the numerical accuracy of the model, a mesh refinement study is conducted to understand the sensitivity of the fundamental natural frequency of the system to the nominal mesh size. The mesh is generated using 8 node brick elements with full integration (C3D8 Abaqus elements). The results are presented in Table 2. The initial mesh size of 0.4 mm is chosen to achieve qualitatively reasonable resolution. The fundamental natural frequency decreases with mesh size, as expected, with changes on the order of 0.1%. A mesh size of 0.30 mm is chosen for the remaining analyses based on computational time considerations and the ability to resolve the fundamental mode frequency.

Table 2: Mesh Refinement Study Results

Nominal Mesh Size (mm)	Fundamental Natural Frequency (Hz)	Percent Change (%)	Number of Nodes
0.40	2849.1	-	65,741
0.35	2845.5	0.13	90,385
0.30	**2844.8**	**0.02**	**138,256**
0.25	2841.0	0.13	169,722
0.20	2838.3	0.10	382,079

The temporal convergence of the model is verified by allowing the model to settle to equilibrium over a variety of time-step sizes. Because energy dissipation through friction is a mechanism of interest, the effect of the time-step size on frictional energy dissipation is studied to determine convergence. The time-steps are chosen based on information provided by the Abaqus manual regarding automatically calculated stable time-steps. The "Automatic" time-step size is a coarse step calculated within Abaqus and is based on the more conservative "1×" time-step size. This "1×" time-step is also automatically calculated by the FEA code as a function of the CFL (Courant-Friedrichs-Lewy) condition. Subsequent refinements of that time-step are listed as "2×" and "3×," respectively. The results of the time-step refinement study are shown in Table 3. It is determined that the "2×" time-step is sufficiently refined for the purposes of capturing the frictional energy dissipation in the joint.

Table 3: Time-Step Refinement Study Results

Description	Time Step (ns)	Frictional Dissipation (mJ)	Percent Change (%)
Automatic	15.9	3.1	-
1×	10.5	3.5	15.5
2×	**5.3**	**3.3**	**7.9**
3×	3.5	3.3	0.98

B. Model Calibration

Several parameters of the model are calibrated based on available materials data. The 4340 steel is assumed to have standard elastic material properties including a modulus of elasticity of 2.05 GPa and Poisson's ratio of 0.29. The part density is 7640 kg/m^3 as determined by a scale. Based on the 8 inch-pounds of experimentally applied bolt torque, the associated preload force within the bolt is calculated to be 266 pounds-force. This is based on standard engineering approximations presented in Budynas and Nisbett [37]. Additionally, the Motosh equation from Bickford [38] yields comparable results. Based on previous analysis for a similar structure under the same fluid dynamic loading in the present shock tube [36], the coefficient of friction used to model frictional contact in the jointed interface is taken to be 0.5. As discussed subsequently, under high-amplitude forcing, the beam response to vortex shedding is quite sensitive to this parameter.

C. Comparison of Modeled and Measured Linear Modes

The first four natural frequencies of the model are compared with experimentally observed natural frequencies from modal testing. The modal testing uses a Maul-Theet automatic impact hammer and a Polytec scanning laser doppler vibrometer (LDV). The modal test is conducted with the beam mounted in the shock tube as in the experiment,

but with a sidewall removed to facility hammer placement (Fig. 9a). The back plate is impacted with a force of 5 N, which is sufficient to excite modes measured on the front and top face of the shell with the LDV. The resulting measured complex mode indicator function (CMIF) [39] is shown Fig. 9b. In short, the CMIF essentially captures the multiple frequency response functions (FRFs) obtained in the LDV scan and thus has same output / input units as a FRF. As labeled in Fig. 9, four primary modes are identified for frequencies less than 5 kHz. The measured mode frequencies and damping coefficients are listed in Table 4. Since the rocking mode appears as a broad plateau an approximate frequency range is listed instead of a discrete value.

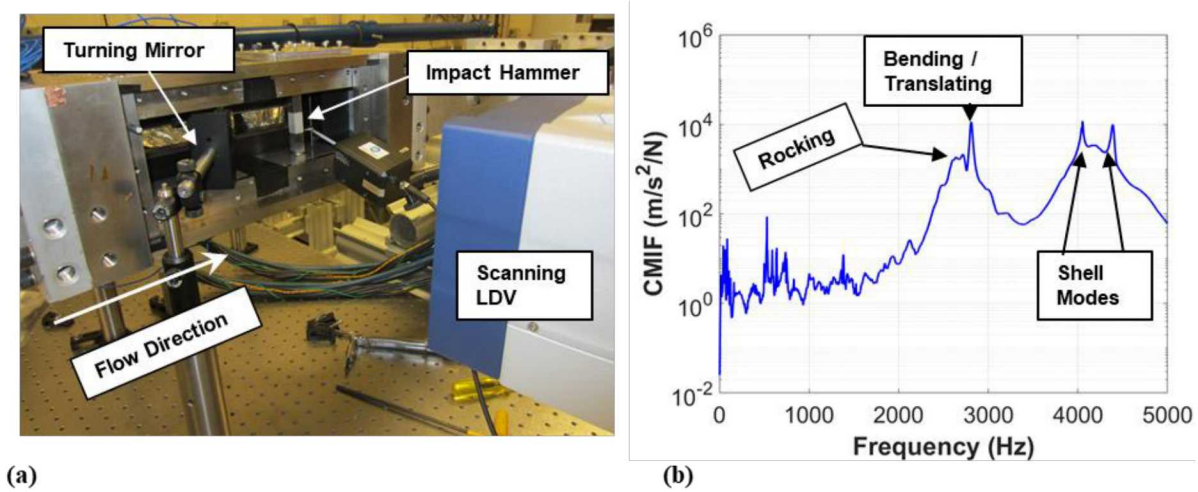

Fig. 9 Modal testing: a) photo of the experimental setup and b) CMIF with description of four most energetic linear modes.

The four primary mode shapes from the linearized finite element model are illustrated in Fig. 10. Importantly, these shapes were determined to be in good visual agreement with the experimentally extracted mode shapes. The two shell modes (Fig. 10c and Fig. 10d) are straightforward to interpret. The rocking mode (Fig. 10a) occurs with bending of the inner jointed connection with imparts some bending onto the back plate (not shown here). The data obtained during shock tube runs show a pronounced streamwise translation of the shell (e.g., Fig. 7a). The modeled 'bending-translating' mode (Fig. 10b) suggests that this translation is primarily due to bending of the back plate and not slip at the joint interface. Thus, the modeling concurrent with experiment allows the influence of the back plate on the two primary structural modes to be discerned. Table 4 compares the experimental and numerical natural frequencies. These results show there to be relatively good agreement between the model and the experiment. The higher modeled natural frequencies are most likely due to excessive stiffness of the fixed model boundary condition compared to the more compliant boundary condition in the experimental apparatus.

Table 4: Measured and Modeled Linear Modes

Mode Description	Experimental Damping (%)	Experimental Frequency (Hz)	Model Frequency (Hz)	Percent Difference (%)
Rocking	2720	2480-2720	2880	+6-14
Bending-translating	0.5	2810	3050	+8
Out-of-Phase Shell	4050	4050	4140	+2
In-Phase Shell	4390	4390	4380	0

V. Results and Discussion

A. Comparison of Experiment and Simulation

Streamwise displacements for a100-psi run are compared in Fig. 11a. The traces are averages of the four available runs. In the case of the modeled response, the simulation was run four times using the four separate PSP loading inputs. Over the first 1.5 ms, the agreement between the experiment and model is relatively poor. This in part due to light refraction effects occurring at early times, which can lead to experimental bias errors of 10s of microns; however,

at later times greater than about 3 ms, the agreement continues to suffer. A comparison of power spectral densities (PSDs) is shown in Fig. 11b. Each PSD is computed in an identical fashion using the Welch windowing algorithm (*pwelch* function) in Matlab. Both the experimental and modeled PSDs show prominent peaks at the bending-translating and shell mode frequencies identified in the modal test and linear modeling. However, the PSD amplitudes vary by about 50%. Collectively, these results suggest the model may be missing a forcing present in the experiment. The fact that the experimental amplitude associated with the bending-translating mode is higher than that in the model may indicate that loading on the back side of the beam is an important driver of this structural mode. Nevertheless, attention now turns to the transverse displacements, which will be shown to be a much stronger driver of nonlinear response in the present work.

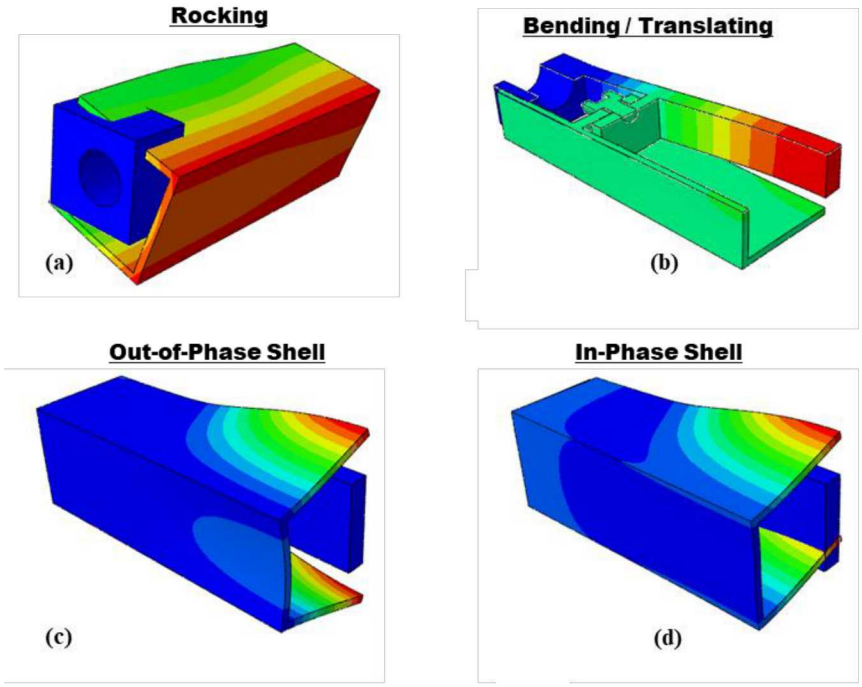

Fig. 10 Primary mode shapes returned by the linearized finite element model: a) rocking mode b) bending-translating mode, c) out-of-phase shell mode and d) in-phase shell mode.

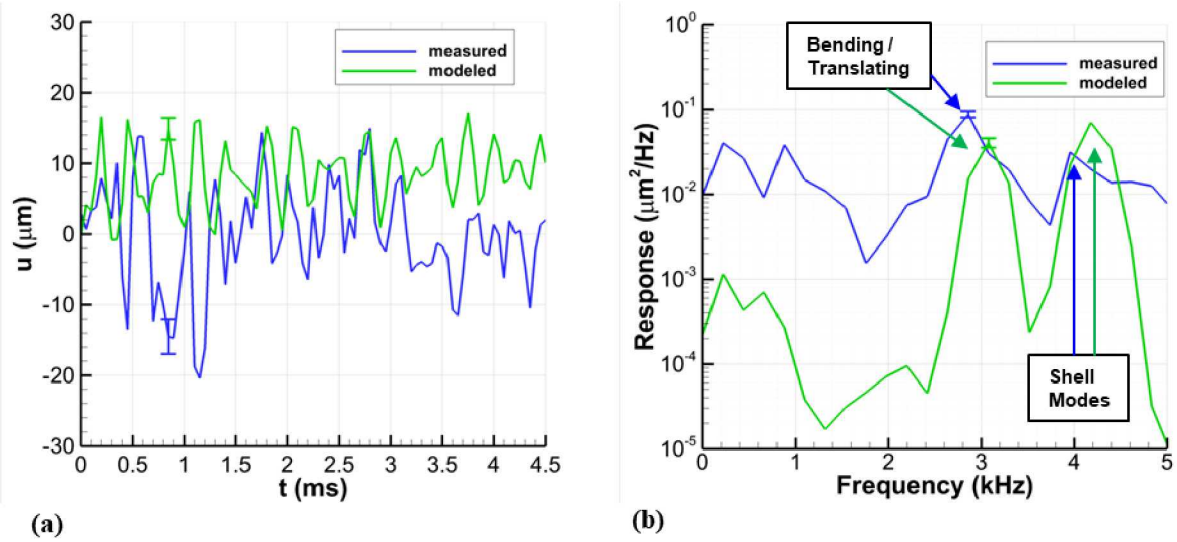

Fig. 11 Comparison of measured (blue) and modeled (green) streamwise displacements during a 100-psi run: a) averaged time-traces and b) averaged PSDs. The error bars here and throughout this section represent the standard error (precision uncertainty).

PSDs of the fluid dynamic forcing, measured displacement and modeled displacement in the transverse direction are compared as function of driver pressure in Fig. 12. The forcing signal is defined to be ΔP (e.g., Fig. 5b). At 50 psi (Fig. 12a), the maximum transverse response occurs at the frequency corresponding to maximum fluid forcing, namely the vortex shedding frequency. The modeled peak displacements are in excellent agreement with the experiment. Additionally, a smaller peak appears in both the modeled and experimental spectra (label A) at the natural frequency of the rocking mode. As the driver pressure increases to 75 psi (Fig. 12b), the vortex shedding frequency increases as expected. Once again, the experimental and modeled spectra exhibit the greatest amplitude at the vortex shedding frequency and a peak at the rocking mode frequency (label B) remains. The response in this case, however, is much greater owing to the marked increase in vortex shedding strength. Moving to a driver pressure of 100 psi (Fig. 12c), results in a decrease in fluid dynamic forcing, but similar observations regarding the structural response curves remain. Peaks are present at the forcing frequency and the rocking mode frequency (label C). At the three driver pressures discussed thus far, $St \approx 0.14$, which is consistent with measurements by Okajima [40], albeit at lower Re_D.

The v-component displacement spectra exhibit distinctive characteristics as the driver pressure is increased further. At 125 psi (Fig. 12d), the vortex shedding amplitude is greatest at 2.2 kHz $< f <$ 2.9 kHz. This range of frequencies contains the entire range of the structural rocking mode as determined from the impact hammer experiment (Fig. 9b, Table 4). This frequency range also contains the rocking mode in the Abaqus model, which has its natural frequency at 2.9 kHz. As a result, both the experimental and modeled displacement spectra exhibit maxima at the rocking mode frequency. At the maximum driver pressure of 150 psi (Fig. 12e), the vortex shedding frequency increases to 3.1 kHz. In contrast to the previous cases, the structural response no longer peaks at the fluid forcing frequency. Rather, the maximum modeled and measured displacements occur at 2.9 kHz near the rocking natural frequency. Notably, this is also the frequency of the bending-translating mode in the experiment. It is possible that this primarily streamwise mode also influences the interaction. The Strouhal number at the two highest driver pressures shifts to 0.16, noticeably higher than at the lower driver pressures. It is possible that the structural dynamics are influencing the pressure field in these cases such that two-way-coupling may be occurring.

Despite the complexity of the present FSI, the modeling and experiment show similar trends. A comparison of v-component PSD amplitudes is shown in Fig. 12f as a function of dynamic pressure. As expected, both the model and experiment show an overall trend of increasing response with increasing q_∞. The maximum response in the experiment occurs in the 125-psi driver case since the fluid and structural frequencies are most closely matched at these conditions. On the other hand, the modeled response shows a maximum in the 150-psi driver case, possibly because the rocking mode natural frequency is greater in the model than in the experiment. The near match of the vortex shedding frequency and the bending-translating mode frequency in the model may also be a factor. The ≈ 10% difference in natural frequency values may be a contributor to discrepancies between the model and experiment in the 150-psi driver case. Naturally, the response could be quite sensitive to the proximity of structural modes to forcing frequencies.

An analogous comparison of time traces as a function of driver pressure is displayed in Fig. 13a - Fig. 13e, where each trace is the time-average of the four available runs. Additionally, transverse displacement fluctuation levels are summarized in the root-mean-square (*rms*) plot of Fig. 13f. Excellent agreement in amplitude and phase is observed at the lowest driver pressure (Fig. 13a). At 75 psi (Fig. 13b) and 100 psi (Fig. 13c), the phase agreement remains excellent while the model under predicts displacement by ≈ 25% (Fig. 13f). The model captures the envelope variation trends at these pressures (e.g., the decreasing amplitude at 100 psi for times greater than 1.5 ms). Similar observations can be made as the driver pressure increases to 125 psi (Fig. 13f). The measured and modeled *rms* levels agree to within ≈ 10% (Fig. 13f) and a decreasing envelope is observed at times greater than 1.2 ms. There is, however, a phase difference between the model and experiment that grows within increasing time. A similar, though more pronounced phase difference can be seen at 150 psi (Fig. 13e). In contrast to the lower driver pressures, there is a phase difference between the experimental forcing and response traces at 125 psi and 150 psi. This phase difference possibly stems from the proximity of the forcing and structural natural frequencies discussed previously. On average, the *rms* levels of the experiment and model agree to within 24%. This and the fact that the model captures the overall trends of the experiment quite nicely lends confidence to using FEA to elucidate nonlinear joint dynamics during the interaction.

B. Nonlinear Dynamics of the Jointed-Structure under FSI

Using the verified, calibrated, and validated model, several additional simulations are run to investigate the nonlinear structural dynamics and the effect of friction on the response under shock- and fluid-dynamic loading. The experimental pressure load from a 125-psi driver test (e.g., Fig. 13d) is applied to the model. Notably, this case represents the highest experimental response where the structural natural frequencies most closely match the fluid. Based on the subsequent examination of the modal participation factors, it is observed that the shock wave loading on the front face tends to actuate the translating-bending mode depicted in Fig. 10b. In contrast, as the flow develops and vortex shedding occurs, the oscillatory pressures on the top and bottom faces drive the rocking mode of Fig. 10a.

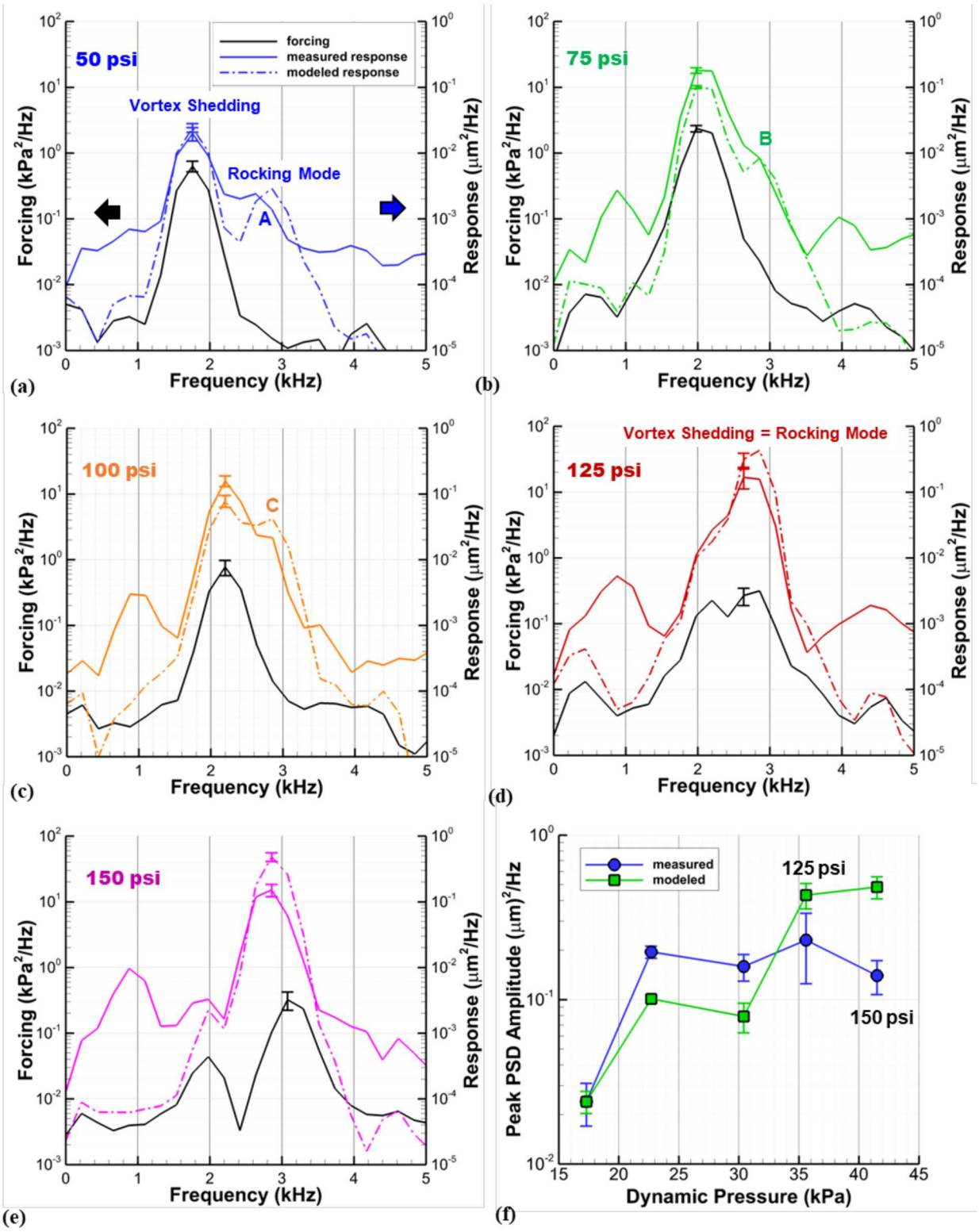

Fig. 12 Comparison of measured and modeled response in the transverse direction as a function of driver pressure: a) PSDs at 50 psi, b) 75 psi, c) 100 psi, d) 125 psi, e) 150 psi and f) comparison of maximum PSD amplitude over all driver pressures. In the PSD subfigures, the forcing spectrum corresponds to the left ordinate and the response to the right. Fluid forcing is shown with black lines, measured response with solid lines and modeled response with dashed lines.

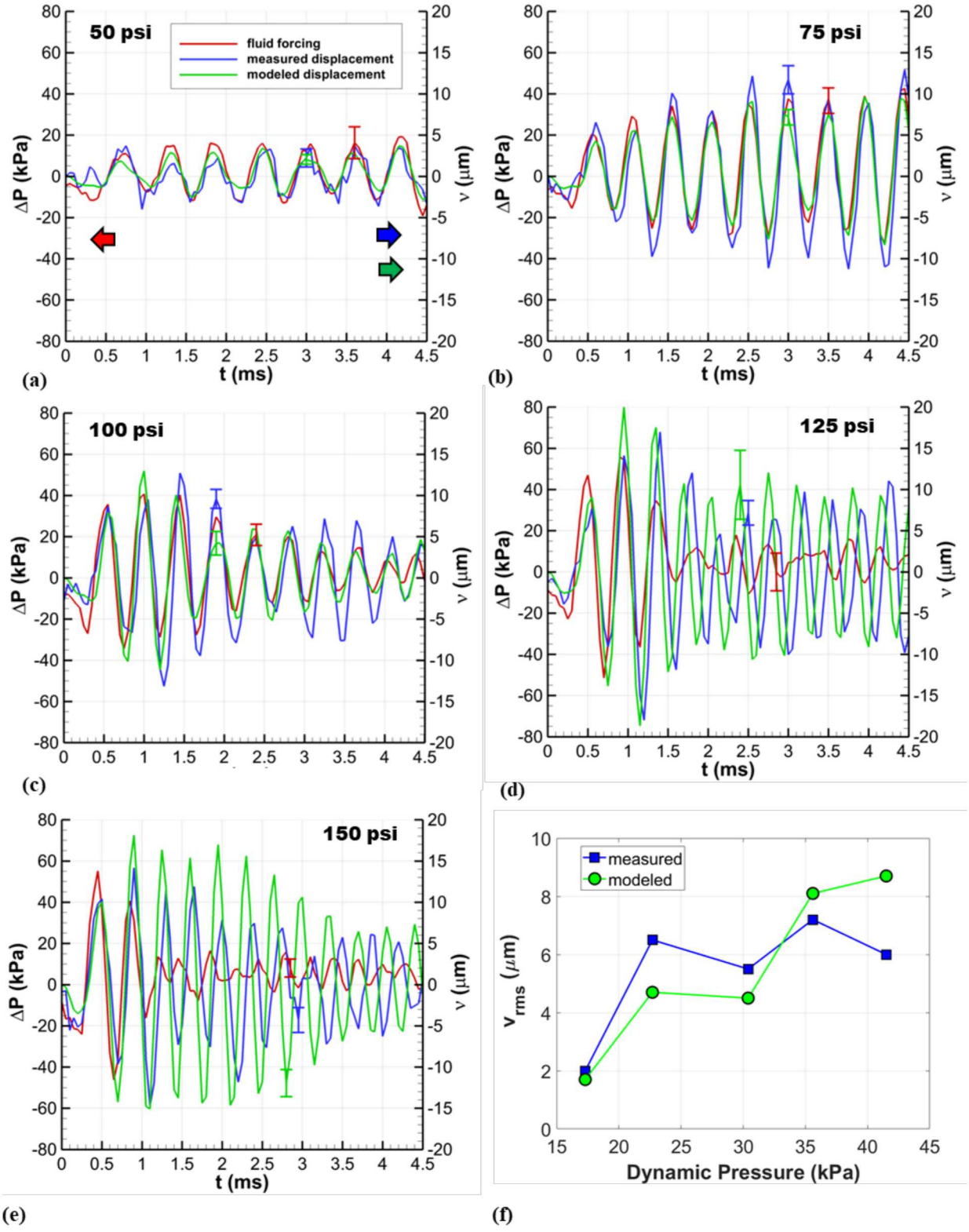

Fig. 13 Comparison of measured and modeled response in the transverse direction as a function of driver pressure: a) time traces at 50 psi, b) 75 psi, c) 100 psi, d) 125 psi, e) 150 psi and f) comparison of maximum root-mean-square fluctuation over all driver pressures. In the time trace subfigures, the forcing spectrum corresponds to the left ordinate and the response to the right. Fluid forcing is shown in red, measured response in blue and modeled response in green.

Several simulations are run while varying the coefficient of friction in the joint interface. The effect of changing the coefficient of friction on the modal energy profile is shown for the first four most energetic modes is shown in Fig. 14. The modal energy is calculated by decomposing the response of the system into modal coordinates as follows:

$$\underline{q} = \Phi^T \underline{u} \tag{3}$$

where $\underline{q}$ is the vector of modal coordinates, $\underline{u}$ is the vector of displacements, and Φ is the modal matrix calculated using Abaqus. The energy in each mode, E_i, is the calculated according to:

$$E_i = \frac{1}{2}\dot{q}_i + \frac{1}{2}\omega_i^2 q_i^2 \tag{4}$$

where q_i is the modal coordinate for the i-th mode, dots denote time derivatives and ω_i is the natural frequency of the i-th mode.

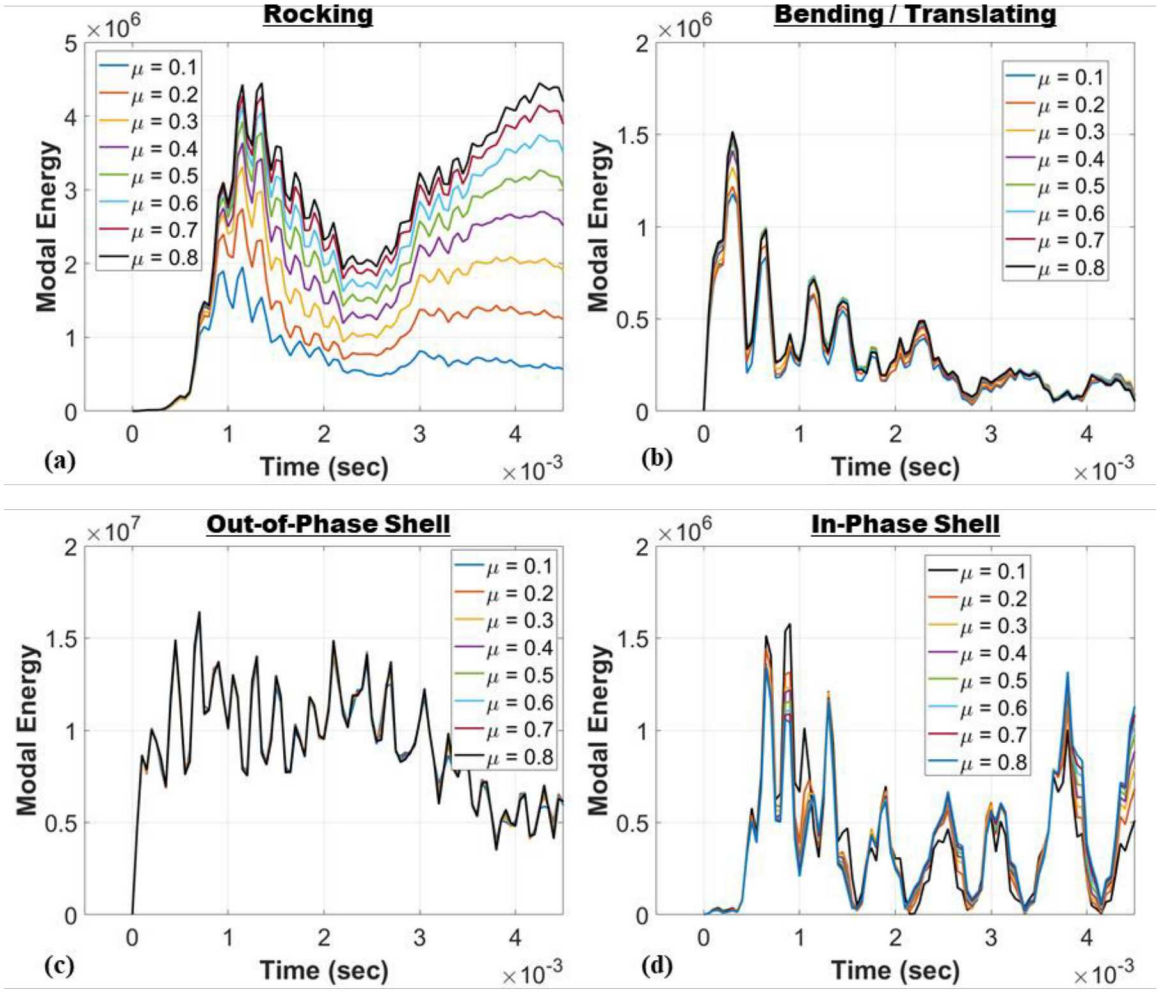

Fig. 14 Primary mode shapes returned by the linearized model: a) rocking mode b) bending-translating mode, c) out-of-phase shell and d) in-phase shell.

This analysis shows that the rocking mode (Fig. 14a) is most significantly affected by changing the nonlinear interface properties of the structure, whereas the other modes are relatively unaffected. The bending and shell modes are roughly invariant with respect to the interface properties as these modes either do not impart significant loads in the joint, or the modes are not driven enough in the shock tube to sustain frictional loss. In contrast, the rocking mode

imparts a significant torque on the jointed interface, thus causing frictional slip which contributes to changes in stiffness and damping for the mode. Specifically, the modal energy is on average about three times greater when μ = 0.8 case in comparison to when μ = 0.1. This result implies that the rocking mode is by far the most pertinent to the nonlinear damping and energy dissipation in the structure. Since the vortex shedding of the fluid drives the response amplitude of the rocking mode, it can be concluded that this fluid dynamic mechanism is most responsible for causing the nonlinear energy dissipation in the structure.

Additional, interesting observations can be made regarding the effects of the impulsive start of the shock tube flow on the structure. Analogous to a hammer impact, the bending-translating (Fig. 14b) and the out-of-phase shell (Fig. 14c) modes begin immediately upon arrival of the air-shock. Contrastingly, the rocking and in-phase shell modes take about 0.5 ms ($\approx 10t^*$) to ramp up as the vortex shedding initiates. Altogether, these results highlight the potential importance of nonlinear structural dynamics under unsteady aerodynamic loading conditions.

Conclusions

Experiments and modeling have been used to study the nonlinear dynamics of a jointed-structure in a shock tube with post-shock velocities ranging from about 150 m/s – 220 m/s. The structure was a full-span square cylinder with internal bolted connections designed to be excited by vortex shedding, which occurred over a frequency range of 1.9 kHz – 3.2 kHz. The Reynolds number based on cylinder width was on the order of 10^5. In the shock tube, the cylinder was exposed to an impulsive, longitudinal force associated with the incident shock wave followed by transverse loading associated with vortex shedding.

In the experiment, aerodynamic loading was characterized with high-speed PSP, while DIC, sensitive to displacements of only a few microns, concurrently measured the structural response. Combined analysis of the PSP and DIC data allowed the amplitude and phase coupling between the transverse force and beam response to be investigated. The simultaneous aspect of the measurement was critical in identifying the relationships between loading and response for the different conditions. The maximum cylinder displacement occurred when then vortex shedding frequency most closely matched the structural natural frequency of the beam associated with rocking motion at the joint.

A finite element model of the system was developed using Abaqus with the goal of investigating the nonlinear structural dynamics of the cylinder under fluid-dynamic loading. Nonlinear dissipation at the internal joint interface was simulated using Coulomb friction. The model returned linear structural mode frequencies that agreed with those measured via an impact hammer to within ≈ 10%. Differences were attributed to modeled boundary conditions, which were treated as perfectly fixed where the structure attached to the shock tube walls. The pressures measured with PSP were averaged over each face of the cylinder and used to load the finite element model. Additionally, the FSI was assumed to be one-way-coupled such that the structural displacements did not influence the flow-field.

With these assumptions, the simulations were able to match the overall trends observed in the experiment. Overall, good phase agreement between the experiment and model was achieved. Furthermore, the transverse structural displacement levels agreed to within about 24% on average. The validated model was then used to study the nonlinear structural dynamics during the FSI. Rocking about the joint interface during vortex shedding was found to be critical to the nonlinear damping and energy dissipation in the structure. More specifically, the modal energies associated with this nonlinear mode varied by a factor of three depending on the value chosen for the coefficient of friction.

Collectively, this combined experimental-modeling study highlights the potential importance of jointed-connections to energy dissipation under FSI loading. An understanding of energy transfer through structural load paths is critical for accurate predictions of structural response.

Acknowledgements

Seth Spitzer and Paul Farias are kindly acknowledged for their support in model preparation including application of the PSP and machining. Tom Grasser is thanked for his help with the experimental model design. We thank Daniel Rohe for performing the linear modal experiments.

Sandia National Laboratories is a multimission laboratory managed and operated by National Technology & Engineering Solutions of Sandia, LLC, a wholly owned subsidiary of Honeywell International Inc., for the U.S. Department of Energy's National Nuclear Security Administration under contract DE-NA0003525. This paper describes objective technical results and analysis. Any subjective views or opinions that might be expressed in the paper do not necessarily represent the views of the U.S. Department of Energy or the United States Government.

References

[1] Sarpkaya, T., "A Critical Review of the Intrinsic Nature of Vortex-Induced Vibrations," *Journal of Fluids and Structures*, Vol. 19, No. 4, 2004, pp. 389-447.

[2] Wagner, J. L., Casper, K. M., Beresh, S. J., Hunter, P. S., Spillers, R. W., and Henfling, J. F., "Response of a Store with Tunable Natural Frequencies in Compressible Cavity Flow," *AIAA Journal*, Vol. 54, No. 8, 2016, pp. 2351-2360.

[3] Blackman, D. R., Clark, D. M., McNulty, G. J., and Wilby, J. F., "Boundary Layer Pressure Fluctuations and Structural Response, Technical Report AFFDL-TR-67-97, Air Force Flight Dynamics Laboratory, October 1967.

[4] Casper, K. M., Beresh, S. J., Henfling, J. F., Spillers, R. W., Hunter, P. S., and Spitzer, S M., "Hypersonic Fluid-Structure Interactions on a Slender Cone," AIAA Paper 2018-1825, January 2018.

[5] Currao, G., Neely, A. J., Buttsworth, D. R., and Choudhury, R., "Measurement and Simulation of Hypersonic Fluid-Structural Interaction on a Cantilevered Plate in a Mach 6 Flow, AIAA Paper 2016-1088, January 2016.

[6] Maestrello, L., and Linden, T. L. J., "Measurements of the response of a panel excited by shock boundary-layer interaction," *Journal of Sound and Vibration*, Vol. 16, No. 3, 1971, pp. 385-391.

[7] Willems, S., Gülhan, A., and Esser, B., "Shock induced fluid-structure interaction on a flexible wall in supersonic turbulent flow," *Progress in Flight Physics*, Vol. 5, 2013, pp. 285-308.

[8] Perez, R., Bartram, G., Beberniss, T., Wiebe, R., and Spottswood, S. M., "Calibration of Aero-Structural Reduced Order Models Using Full-Field Experimental Measurements," *Mechanical Systems and Signal Processing*, Vol. 86, 2017, pp.49-65.

[9] Maestrello, L., "Control of Shock Loading from a Jet in a Flexible Structure's Presence," *AIAA journal*, vol. 38, no. 6, 2000, pp. 972-977.

[10] Hortensius, R., Dutton, J. C., and Elliott, G. S., "Simultaneous Planar PIV and sDIC Measurements of an Axisymmetric Jet Flowing Across a Compliant Surface," AIAA Paper 2017-1886, January 2017.

[11] Dowell, E. H., "Panel Flutter-A Review of the Aeroelastic Stability of Plates and Shells," *AIAA Journal*, Vol. 8, No. 3, 1970, pp. 385-399.

[12] Gaul, L., and Lenz, J., "Nonlinear Dynamics of Structures Assembled by Bolted Joints," *Acta Mechanica*, Vol. 125, No. 1-4, 1997, pp. 169-181.

[13] Gaul, L., and Nitsche, R., "The Role of Friction in Mechanical Joints," *Applied Mechanics Reviews*, Vol. 54, No. 2, 1991, pp. 93-106.

[14] Brake, M.R., "An Overview of Constitutive Models," In *The Mechanics of Jointed Structures*, Springer, Cham, 2018, pp. 207-221.

[15] Segalman, D. J., "A Four-Parameter Iwan Model for Lap-Type Joints, *Journal of Applied Mechanics*, Vol. 72, No. 5, 2005, pp. 752-760.

[16] Iwan, W. D., "A Distributed-Element Model for Hysteresis and its Steady-State Dynamic Response," *Journal of Applied Mechanics*, Vol. 33, No. 4, 1966, pp. 893-900.

[17] De Wit, C. C., Olsson, H., Astrom, K. J., and Lischinsky, P., "A New Model for Control of Systems with Friction," *IEEE Transactions on Automatic Control*, Vol. 40, No. 3, 1995, pp. 419-425.

[18] Liu, T., Burner, A. W., Jones, T. W. and Barrows, D. A., "Photogrammetric Techniques for Aerospace Applications," *Progress in Aerospace Sciences*, Vol. 54, 2012, pp.1-58.

[19] Flaherty, W., Reedy, T. M., Elliott, G. S., Austin, J. M., Schmit, R. F. and Crafton, J., "Investigation of Cavity Flow using Fast-Response Pressure-Sensitive Paint," *AIAA Journal*, Vol. 52, No. 11, 2012, pp.2462-2470.

[20] Sellers, M., Nelson, M. and Crafton, J. W., "Dynamic Pressure-Sensitive Paint Demonstration in AEDC Propulsion Wind Tunnel 16T," AIAA Paper 2016-1146, January 2016.

[21] Beberniss, T. J., Spottswood, S. M., Erhhardt, D. A., and Perez, R., "Nonlinear Response of a Thin Panel Subjected to a Shockwave Impingement and Thermal Buckling, AIAA Paper 2017-3555, June 2017.

[22] Spottswood, S.M., Eason, T., and Beberniss, T., "Full-field, Dynamic Pressure and Displacement Measurements of a Panel Excited by Shock Boundary Layer Interaction, AIAA Paper 2013-2016, May 2016.

[23] Ogg, D. R., Rice, B. E., Peltier, S. J., Staines, J. T., Claucherty, S. L. and Combs, C. S., "Simultaneous Stereo Digital Image Correlation and Pressure-Sensitive Paint Measurements of a Compliant Panel in a Mach 2 Wind Tunnel," AIAA Paper 2018-3869, June 2018.

[24] Armstrong-Hélouvry, B., Dupont, P., and De Wit, C. C., "A Survey of Models, Analysis Tools and Compensation Methods for the Control of Machines with Friction, *Automatica*, Vol. 30, No. 7, 1994, pp. 1083-1138.

[25] Pitenis, A. A., Dowson, D., and Sawyer, W. G., "Leonardo da Vinci's Friction Experiments: An Old Story Acknowledged and Repeated," *Tribology Letters*, 56(3), 2014, pp. 509-515.

[26] Wagner, J. L., Beresh, S .J., Kearney, S. P., Trott, W. M., Castaneda, J. N., Pruett, B. O. and Baer, M. R., "A Multiphase Shock Tube for Shock Wave Interactions with Dense Particle Fields," *Experiments in Fluids*, Vol. 52, No. 6, 2012, pp.1507-1517.

[27] Mirels, H., "Shock Tube Test Time Limitation due to Turbulent Wall Boundary Layer," *AIAA Journal*, Vol. 2, No. 1, 1964, pp. 84-93.

[28] Wagner, J. L., DeMauro, E. P., Casper, K. M., Beresh, S. J., Lynch, K. P., and Pruett, B. O., "Pulse-Burst PIV of an Impulsively Started Cylinder in a Shock Tube for Re > 10^5, *Experiments in Fluids*, Vol. 59, No. 6, 2018, pp. 106.

[29] Egami, Y., Sato, Y., and Konishi, S., "Development of Polymer/Ceramic Pressure-Sensitive Paint with the same response time as Anodized-Aluminum PSP," AIAA Paper 2018-1032, January 2018.

[30] Gregory, J. W., Sakaue, H., Liu, T., and Sullivan, J. P., "Fast Pressure-Sensitive Paint for Flow and Acoustic Diagnostics, *Annual Review of Fluid Mechanics*, Vol. 46, 2014, pp. 303-330.

[31] Bell, J. H., and McLachlan, B. G., "Image Registration for Pressure-Sensitive Paint Applications," *Experiments in Fluids*, Vol. 22, No. 1, 1996, pp. 78-86.
[32] Venkatakrishnan, L., "Comparative Study of Different Pressure-Sensitive-Paint Image Registration Techniques," *AIAA Journal*, Vol. 42, No. 11, 2004, pp. 2311-2319.
[33] Bell, J. H., Schairer, E. T., Hand, L. A., and Mehta, R. D., "Surface Pressure Measurements using Luminescent Coatings," *Annual Review of Fluid Mechanics*, Vol. 33, No. 1, 2001, pp. 155-206.
[34] Taira, K., Brunton, S. L., Dawson, S. T., Rowley, C. W., Colonius, T., McKeon, B. J., Schmidt, O. T., Gordeyev, S., Theofilis, V., and Ukeiley, L. S., 2017, "Modal Analysis of Fluid Flows: An Overview," *AIAA Journal*, 2017, pp. 4013-4041.
[35] Lynch, K. P., Jones, E. M., and Wagner, J. L., "Simultaneous PSP and Surface Deformation Measurements for Fluid-Structure Interactions in a Shock Tube," AIAA Paper 2018-3870, June 2018.
[36] Mathis, A., Akron Dissertation (2019)
[37] Budynas and Nisbett (2011)
[38] Bickford (2008)
[39] Hensley D. P. and Mayes, R. L., "Extending SMAC to Multiple Reference FRFs," in Proceedings of the 24th International Modal Analysis Conference, pp. 220-230, Jan. 2006.
[40] Okajima, A., "Strouhal Numbers of Rectangular Cylinders," *Journal of Fluid Mechanics*, Vol. 123, No. 10, 1982, pp. 379-398.